Earth and Planetary Science Letters 479 (2017) 108–119

Contents lists available at ScienceDirect

Earth and Planetary Science Letters

www.elsevier.com/locate/epsl

Disequilibrium growth of olivine in mafic magmas revealed by phosphorus zoning patterns of olivine from mafic–ultramafic intrusions

Chang-Ming Xing [a,b], Christina Yan Wang [a,b,*], Wei Tan [a,b]

[a] Key Laboratory of Mineralogy and Metallogeny, Guangzhou Institute of Geochemistry, Chinese Academy of Sciences, Guangzhou 510460, China
[b] Guangdong Provincial Key Laboratory of Mineral Physics and Materials, Guangzhou 510640, China

ARTICLE INFO

Article history:
Received 27 March 2017
Received in revised form 18 August 2017
Accepted 6 September 2017
Available online 2 October 2017
Editor: M. Bickle

Keywords:
olivine
phosphorus zoning
disequilibrium texture
igneous cumulate
mafic–ultramafic intrusion

ABSTRACT

Olivine from mafic–ultramafic intrusions rarely displays growth zoning in major and some minor elements, such as Fe, Mg and Ni, due to fast diffusion of these elements at high temperatures. These elements in olivine are thus not useful in deciphering magma chamber processes, such as magma convection, multiple injection and mixing. High-resolution X-ray elemental intensity mapping reveals distinct P zoning patterns of olivine from two mafic–ultramafic intrusions in SW China. Polyhedral olivine grains from lherzolite and dunite of the Abulangdang intrusion show P-rich dendrites similar to those observed in volcanic rocks. Rounded olivine grains from net-textured Fe–Ti oxide ores of the Baima layered intrusion have irregular P-rich patches/bands crosscut and interlocked by P-poor olivine domains. P-rich patches/bands contain 250 to 612 ppm P, much higher than P-poor olivine domains with 123 to 230 ppm P. In electron backscattered diffraction (EBSD) maps, P-rich patches/bands within a single olivine grain have the same crystallographic orientation, indicating that they were remnants of the same crystal. Thus, both P-rich patches/bands and P-poor olivine domains in the same grain show a disequilibrium texture and clearly record two-stage growth. The P-rich patches/bands are likely the remnants of a polyhedral olivine crystal that formed in the first stage, whereas the P-poor olivine domains containing rounded Ti-rich magnetite and Fe-rich melt inclusions may have formed from an Fe-rich ambient melt in the second stage. The complex P zoning of olivine can be attributed to the dissolution of early polyhedral olivine and re-precipitation from the Fe-rich ambient melt. The early polyhedral olivine was in chemical disequilibrium with the ambient melt that may have been developed by silicate liquid immiscibility in a crystal mush. Our study implies that olivine crystals in igneous cumulates with an equilibrium appearance may have experienced disequilibrium growth processes during slow cooling. Therefore, the crystallization sequence of mafic magmas based on textural relationships should be treated with caution.

1. Introduction

Olivine usually crystallizes as an early phase in mafic magmas. It has a simple chemical formula [$(Fe, Mg)_2SiO_4$] and diverse crystal habits including polyhedral, skeletal, dendritic, rounded and spongy shapes (Helz, 1987; Welsch et al., 2013), depending on different cooling rates and degrees of undercooling (Donaldson, 1976; Jambon et al., 1992; Faure et al., 2003, 2007; Faure and Schiano, 2004). Elucidation of the growth processes of olivine has important implications for crystal growth mechanisms, magma evolution and magma chamber processes (Sobolev et al., 2007; Pilbeam et al., 2013; Sanfilippo et al., 2014).

Olivine growth is diffusion-controlled during rapid cooling when it forms skeletal or dendritic crystals (Faure et al., 2003, 2007; Faure and Schiano, 2004). Dendrites are commonly preserved in olivine phenocrysts of volcanic rocks and are attributed to initially rapid growth of crystals, followed by slow ripening of hollow crystals during cooling (Milman-Barris et al., 2008; Welsch et al., 2013, 2014). On the other hand, olivine growth during slow cooling forms polyhedral crystals in an interface-controlled, tree-ring or spiral growth model (Burton et al., 1951; Faure and Schiano, 2005; Faure et al., 2007). Therefore, polyhedral olivine crystals in igneous cumulates usually lack growth zoning and sometimes show equilibrium textures such as 120° triple junction of grain boundaries. However, because of fast Mg–Fe diffusion in olivine and post-crystallization processes, e.g., trapped liquid

* Corresponding author at: Key Laboratory of Mineralogy and Metallogeny, Guangzhou Institute of Geochemistry, Chinese Academy of Sciences, Guangzhou 510460, China.
E-mail address: wang_yan@gig.ac.cn (C.Y. Wang).

http://dx.doi.org/10.1016/j.epsl.2017.09.005
0012-821X/

shift effect and sub-solidus re-equilibrium of cumulus minerals in magma chambers (Barnes, 1986; Pang et al., 2008), compositions of primary olivine in igneous cumulates may have been intensely modified. In addition, the mechanism of olivine growth during slow cooling has been relatively neglected and poorly understood. It is thus worthy to examine the growth process of olivine in a deep-seated magma chamber where rapid cooling is unlikely.

Experimental studies reveal that P has an extremely low diffusion rate compared with other elements in olivine (Spandler et al., 2007; Watson et al., 2015), and can be useful in deciphering the growth mechanism of olivine in igneous cumulates. In this paper, we present results of high-resolution X-ray elemental intensity mapping for polyhedral olivine from dunite and lherzolite of the Abulangdang ultramafic intrusion and rounded olivine from net-textured Fe–Ti oxide ores of the Baima layered intrusion in SW China. These results, in combination with those of EBSD mapping and *in situ* analyses by laser inductively coupled-plasma mass spectrometry (LA-ICP-MS), indicate that polyhedral olivine grains from dunite and lherzolite display P zoning patterns identical to those of olivine phenocrysts in volcanic rocks, whereas rounded olivine grains from net-textured Fe–Ti oxide ores have much more complex P zoning patterns that record unusual two-stage growth. This study thus provides new insights into the growth processes of olivine in mafic magmas and has important implications for magmatic processes through which Fe–Ti oxide-rich mafic–ultramafic intrusions formed.

2. Abulangdang and Baima intrusions in SW China

Both the Abulangdang and Baima intrusions in SW China are parts of the Emeishan large igneous province (LIP). The Emeishan LIP is believed to have been formed from a mantle plume at ~260 Ma and covers an area of 7×10^5 km^2 from SW China to northern Vietnam (Li et al., 2017 and references therein) (Fig. 1a). The volcanic succession of the Emeishan LIP varies in thickness from several hundred meters to ~5 km and is mainly composed of low-Ti and high-Ti flood basalts, with minor picrite, tephrite and basaltic andesite (Xu et al., 2001; Qi et al., 2008). There are numerous coeval mafic–ultramafic intrusions and granitic and syenitic plutons in the Emeishan LIP (Zhou et al., 2008; Shellnutt and Iizuka, 2012).

In the Panzhihua–Xichang (Panxi) district, flood basalts of the Emeishan LIP are spatially associated with mafic–ultramafic intrusions and granitic and syenitic plutons that are exposed by several NS-trending faults (Fig. 1b). The mafic–ultramafic intrusions constitute a mineralized belt about 300 km long and 10 to 30 km wide, forming the most important metallogenic district for Fe, Ti and V in China (Zhou et al., 2005). The Abulangdang intrusion is the only ultramafic intrusion in the Panxi region (Wang et al., 2014). The Panzhihua, Baima, Taihe and Hongge layered intrusions host world-class Fe–Ti-(V) oxide deposits, whereas some other small mafic–ultramafic intrusions have Ni–Cu-(PGE) sulfide mineralization (Fig. 1b).

2.1. Abulangdang ultramafic intrusion

The Abulangdang ultramafic intrusion is an elongate lopolith and covers an area of ~7.6 km^2. It is a concentric body composed of an inner core of dunite (75 vol.%) surrounded by plagioclase-bearing lherzolite (15 vol.%) and olivine gabbro (10 vol.%) (Wang et al., 2014) (Fig. 1c). The intrusion was considered to have formed from high-Ti picritic magmas at a depth equivalent to pressure of 7 to 10 kbar (Wang et al., 2014).

The dunite consists of 85 to 95% olivine, 3 to 10% orthopyroxene, <5% clinopyroxene and <2% chromite. Polyhedral olivine crystals have grain sizes ranging from 0.2 to 2 mm and show well-developed 120° triple junction of grain boundaries (Fig. 2a). The lherzolite is composed of 50 to 85% olivine, 5 to 10% clinopyroxene, 5 to 15% orthopyroxene, 5 to 10% plagioclase and <3% chromite and <2% sulfide. Olivine crystals are euhedral to subhedral and vary in size from 0.2 to 5 mm. Some olivine grains are enclosed within clinopyroxene, typical of poikilitic texture (Fig. 2b). Fine-grained chromite crystals are commonly enclosed in olivine (Fig. 2b).

2.2. Baima layered intrusion

The Baima intrusion is ~24 km long and 2 to 6.5 km wide, and contains a large Fe–Ti-(V) oxide deposit in the Panxi region (Fig. 1d). The layered sequence of the intrusion is ~1,600 m thick and is divided into a lower zone and an upper zone (Liu et al., 2014a). The lower zone is ~150 to 300 m thick and is mainly composed of troctolite, olivine clinopyroxenite and olivine gabbro and hosts ~100 m-thick Fe–Ti oxide ore layers. The ore layers are composed of net-textured Fe–Ti oxide ores with 40 to 60% Fe–Ti oxides and disseminated ores with 20 to 40% Fe–Ti oxides (Liu et al., 2014a). The upper zone is up to ~1,200 m in thickness and is composed of isotropic olivine gabbro, gabbro and apatite-bearing gabbro. These rocks usually contain <10% Fe–Ti oxides. The Baima intrusion is proposed to have formed from high-Ti basaltic magmas at a depth equivalent to pressure of 3 to 5 kbar (Shellnutt et al., 2009; Pang et al., 2010). The formation of Fe–Ti oxide ores in the lower zone is thought to be due to silicate liquid immiscibility during the crystallization of the intrusion (Liu et al., 2014b).

Net-textured Fe–Ti oxide ores consist of 40 to 60% Fe–Ti oxides, 30 to 35% olivine, <10% plagioclase, <5% clinopyroxene and <2% sulfide (Fig. 3a). Olivine grains from net-textured ores are commonly rounded or elliptical. They vary from 0.02 to 2 mm in diameter, and are isolated by interconnected matrix composed of Fe–Ti oxides and minor sulfides (Fig. 3a). Olivine grains do not show clear zonation under microscope or in backscattered electron (BSE) images. They contain rounded, Ti-rich magnetite (<200 μm in diameter) and occasionally polycrystalline inclusions (Figs. 3b, c and d). Previous 3-D X-ray CT scanning reveals that the Ti-rich magnetite and polycrystalline inclusions are spherical in shape and are entirely enclosed in olivine, and do not connect with interstitial Fe–Ti oxides (Liu et al., 2014b). The polycrystalline inclusions are mainly composed of Ti-rich magnetite, ilmenite, spinel and phlogopite with sporadic apatite, amphibole and sulfides (Fig. 3d; also see Liu et al., 2014b), and they were explained to be trapped Fe-rich melt inclusions (Liu et al., 2014b). Chlorite commonly occurs along the rims and fractures of olivine (Figs. 3a and b). Plagioclase commonly has an irregular outline and is commonly rimmed by amphibole (Fig. 3a).

3. Analytical methods

3.1. High resolution X-ray elemental intensity mapping using electron microprobe

High resolution X-ray elemental intensity mapping for Mg, Fe, Al, Cr, Ni, Ca and P were applied for olivine grains on carbon-coated thin sections. The X-ray mapping was carried out using a JEOL JXA-8230 electron microprobe at the Key Laboratory of Mineralogy and Metallogeny in Guangzhou Institute of Geochemistry (GIG), Chinese Academy of Sciences (CAS). The operation conditions of an accelerate voltage of 20 kV, a probe current of 300 nA and a beam size of 1 to 4 μm were adopted for mapping. Mg and Al were analyzed using a TAP crystal. Fe, Cr and Ni were analyzed using a LIF crystal. Ca was analyzed using a PET crystal. P was analyzed with a PETH crystal to strengthen X-ray intensity. Elemental Kα line was chosen for all elements during analyses. The

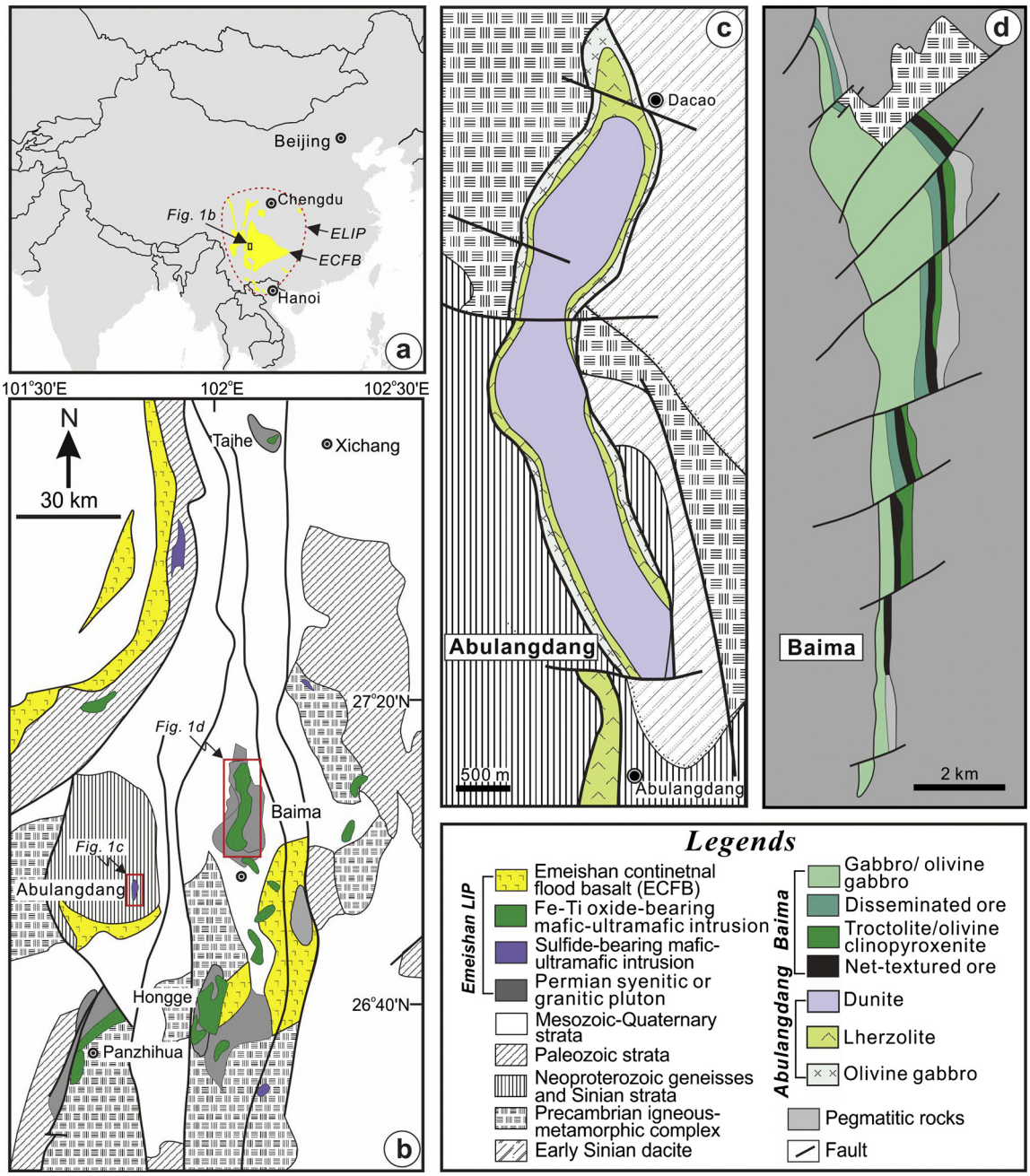

Fig. 1. Geological map showing the distribution of the Emeishan large igneous province (ELIP) and Emeishan continental flood basalts (ECFB) in SW China and northern Vietnam (a) (modified after Xu et al., 2001 and Li et al., 2017) and related mafic–ultramafic intrusions in the Panxi region in SW China (b) (modified after Shellnutt and Iizuka, 2012). (c) Geological map of the Abulangdang ultramafic intrusion (modified after Wang et al., 2014). (d) Geological map of the Baima layered intrusion (modified after Liu et al., 2014b).

step size varied from 1 to 4 μm and the dwell time was set to be 100 to 200 ms for each point. Typically 7 to 16 h were required to accomplish mapping for one grain. P Kα X-ray line scan was obtained using an accelerate voltage of 20 kV, a probe current of 300 nA and a beam size of 1 μm. The step size was set to be 1 μm and the dwell time was increased to 1,000 ms for each point.

3.2. Electron backscattered diffraction (EBSD) mapping

Electron backscattered diffraction mapping was adopted to measure the crystallographic orientation of olivine at the State Key Laboratory of Geological Processes and Mineral Resources in China University of Geosciences (Wuhan) using an Oxford HKL Nordlys II EBSD detector coupled with a FEI Quanta 450 field emission gun scanning electron microscope (FEG-SEM). The analytical procedure was described in Xu et al. (2015). Thin sections were uncoated to obtain better quality of Kikuchi patterns in a low-vacuum mode (30 Pa). The measurements were conducted with an accelerate voltage of 20 kV and a working distance of ~25 mm. The thin sections were tilted 70° and Kikuchi patterns were acquired on rectangular grids by shifting the electron beam with a step size of 10 or 20 μm. The CHANNEL 5+ software was used to remove erroneous, disoriented data from all eight neighboring measurements by more than 5° and to replace non-indexed measuring points with the commonest neighboring orientation, so that introduction of artifacts was avoided in the reconstruction of an orientation map from raw orientation maps.

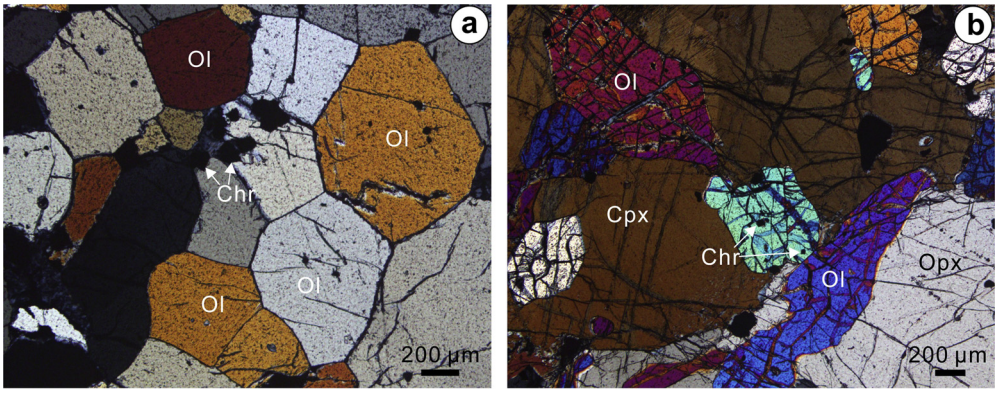

Fig. 2. Photomicrographs of dunite and lherzolite from the Abulangdang intrusion. (a) Polyhedral olivine (Ol) grains in dunite have straight outlines with 120° triple junction among grain boundaries. (b) lherzolite shows poikilitic texture and olivine is enclosed within clinopyroxene (Cpx) and orthopyroxene (Opx). Fine-grained chromite (Chr) is occasionally enclosed in olivine in both rock types. Under cross-polarizer and transmitted light.

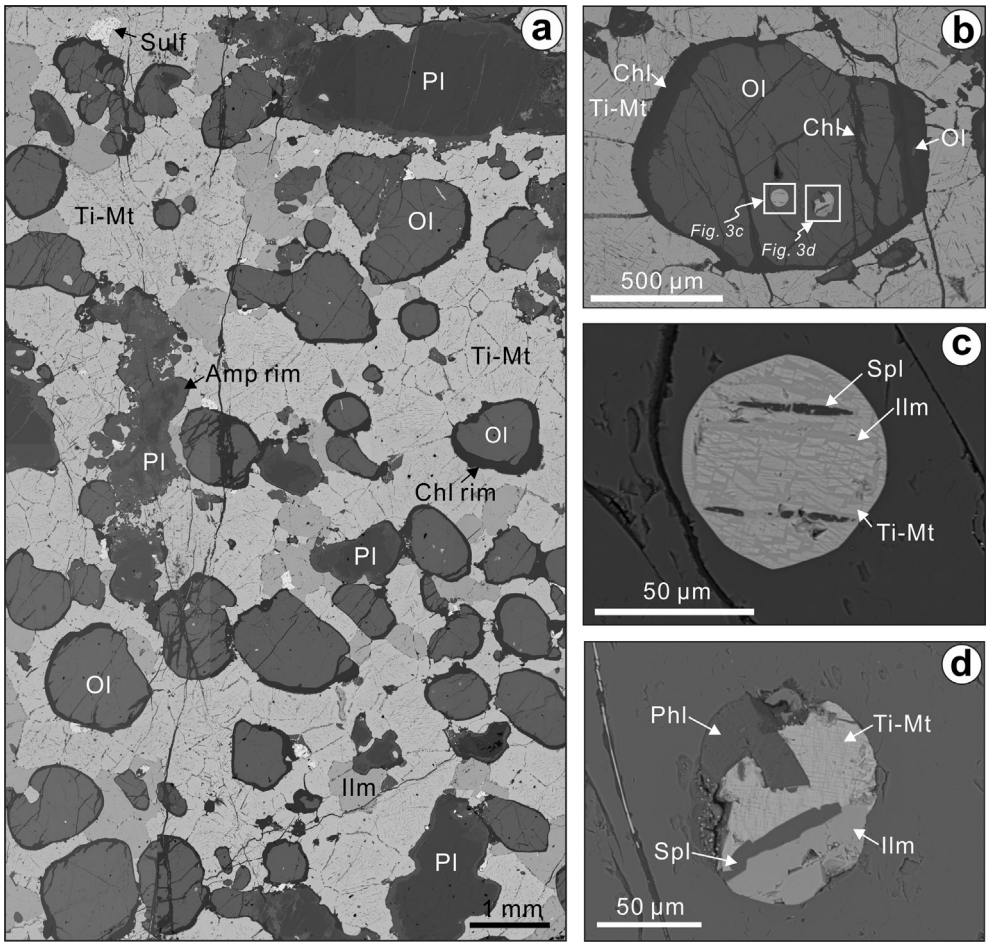

Fig. 3. BSE images of net-textured Fe–Ti oxide ores from the Baima layered intrusion. (a) Rounded olivine (Ol) grains are surrounded by interstitial Ti-rich magnetite (Ti-Mt), ilmenite (Ilm) and minor amounts of sulfide (Sulf). Plagioclase (Pl) primocrysts are resorbed and rimmed by amphibole (Amp). Chlorite (Chl) occurs in the rims and fractures of rounded olivine. (b) Fine-grained Ti-rich magnetite and polycrystalline inclusions are enclosed within rounded olivine. (c) Close-up of Ti-rich magnetite inclusion in Fig. 3b showing nearly rounded outline and exsolution of ilmenite and spinel (Spl). (d) Close-up of polycrystalline inclusion in Fig. 3b, which is composed of Ti-rich magnetite, ilmenite, spinel and phlogopite (Phl).

3.3. Element quantitative analysis

Major elements of olivine were determined using a JEOL JXA-8230 electron probe micro-analyzer (EPMA) at the Key Laboratory of Mineralogy and Metallogeny of GIGCAS. Operating conditions were 15 kV, 20 nA and a 1 μm beam for analyses of all elements. Peak and background counting times were 20 and 10 s for Si, Fe and Mg, 40 and 20 s for Ca and 60 and 30 s for Ni. Analytical results were reduced using the ZAF correction routines. The standards used were olivine for Si and Mg, magnetite for Fe, diopside for Ca, and Ni metal for Ni. Relative precisions are ±2% for Si, Fe and Mg and ±5% for Ca and Ni.

In situ trace element analyses of olivine were carried out using a laser ablation inductively coupled-plasma mass spectrometry (LA-ICP-MS) in the same lab. The Agilent 7500a ICP-MS instrument was coupled to a Resonetic 193 nm ArF excimer laser ablation

system. Single spot ablation was adopted with a laser beam of 31 μm. Laser energy was 80 mJ and ablation frequency was 6 Hz. Helium gas was used as a carrier gas. NIST SRM 610 glass was employed as an external standard and GOR-132 glass was treated as an unknown sample. SiO_2 contents determined by EPMA were used as an internal standard. Data reduction was performed using the ICPMSDataCal software (version 10.2) (Liu et al., 2008). The detection limit is ~22 ppm for P and the analytical uncertainty is better than 10% (relative).

The measured trace element concentrations of NIST SRM 610 and GOR-132 and their recommended values are listed in the Supplementary Table 1. Representative compositions of major and trace elements of olivine from the Abulangdang and Baima intrusions are shown in Table 1. The full dataset is available in the Supplementary Table 2 and Table 3.

4. Results

4.1. P zoning of polyhedral olivine from the Abulangdang intrusion

Two representative samples of lherzolite and dunite from the Abulangdang intrusion were used for X-ray elemental intensity mapping. Polyhedral olivine grains from lherzolite and dunite show nearly homogeneous intensities of Mg, Fe and Al, and variable intensities of Ca that is higher in the cores than rims (Supplementary Fig. 1). In contrast, they contain prominent P-rich dendrites in overall P-poor olivine domains, i.e., P-rich zones are straight and appear as parallel bands, wedge-shaped or concentric zones alternating with P-poor olivine domains (Figs. 4e, f, g and h). P-rich bands vary from ca. 10 to 30 μm in width (Fig. 4). It is noted that P-rich dendrites construct the framework of olivine (Figs. 4i, j, k and l) and that the junctions of P-rich zones have higher P intensities than those along the facet of olivine (Figs. 4f and g). These features are identical to P zoning patterns of olivine phenocrysts in volcanic rocks (Milman-Barris et al., 2008; Welsch et al., 2013, 2014).

P-poor olivine domains of polyhedral olivine grains contain fine-grained chromite inclusions (Fig. 4e). It is notable that P-rich bands near the chromite inclusion are regular and continuous along the crystal face.

4.2. P zoning of rounded olivine from the Baima intrusion

Four representative samples of net-textured Fe–Ti oxide ores from the drill core ZK40-3 of the Baima layered intrusion were used for X-ray elemental intensity mapping. Rounded olivine grains from net-textured Fe–Ti oxide ores have nearly homogeneous intensities of Mg, Fe, Ca, Al, Cr and Ni in the interior of each crystal (Supplementary Fig. 2), whereas P intensities display complex zoning patterns (Fig. 5) that are remarkably different from those of polyhedral olivine grains from the Abulangdang intrusion (Fig. 4). P-rich zones in the overall P-poor olivine domains display diverse patterns, including concentric and wavy bands (Fig. 5e), interlinked patches (Fig. 5f), isolated patches (the upright grain in Fig. 5g) and skeletal branches (Fig. 5h). Concentric, P-rich bands can be truncated by P-poor olivine domains (Fig. 5e). They have variable widths from ~30 to 200 μm and are in sharp contact with P-poor olivine domains in terms of P intensities (Fig. 5i). Irregular, P-rich patches are either interlinked with each other (Fig. 5f) or scattered in P-poor olivine domains (Fig. 5g), both being transitional in terms of P intensities (Fig. 5j). Some small olivine grains show uniform P intensities in the interior but may contain a thin P-poor rim locally (the left grain in Fig. 5f). In some olivine grains, closely spaced, thin bands in P-rich, skeletal branches are preserved (Fig. 5h).

Rounded Ti-rich magnetite and polycrystalline inclusions occur either in P-poor olivine domains or partly in contact with P-rich patches and bands (Figs. 6c and d). P-rich patches and bands near rounded Ti-rich magnetite and polycrystalline inclusions are either highly irregular or truncated by P-poor olivine domains. These features are remarkably different from straight and regular P-rich zones near the chromite inclusion within polyhedral olivine grains from the Abulangdang intrusion (Fig. 4e).

4.3. P concentrations of olivine

Polyhedral olivine grains from lherzolite and dunite of the Abulangdang intrusion have Fo contents ranging from 84 to 88 mol.% (Supplementary Table 2). Within a single olivine grain, Fo and Ni contents are nearly constant, but P concentrations are variable (Fig. 7a). P-rich zones have P concentrations ranging from 95 to 503 ppm, higher than P-poor olivine domains with 45 to 78 ppm P (Supplementary Table 2). Given the thin P-rich zones (10–30 μm) in the polyhedral olivine grains and the large spot size of the laser beam (31 μm), variable P concentrations measured for P-rich zones were likely due to the mixture of P-rich zones and P-poor olivine domains.

Rounded olivine grains from net-textured Fe–Ti oxide ores of the Baima intrusion have Fo contents ranging from 71 to 75 mol.% and the variation of Fo contents is <2 mol.% within a single grain (Supplementary Table 3) (Fig. 7b). P-rich bands and patches of rounded olivine grains have P concentrations varying from 250 to 612 ppm, whereas P-poor olivine domains have 123 to 230 ppm P, much lower than those of P-rich bands and patches (Table 1). Within the same grain, P-rich bands and patches may have P concentrations two to four times higher than P-poor olivine domains, which is in contrast to relatively restricted Fo and Ni contents of the same grain (Fig. 7b).

4.4. Crystallographic orientation of olivine

In the color-coded EBSD orientation map of olivine, different colors would reflect different crystallographic orientations. Rounded olivine grains from net-textured Fe–Ti oxide ores of the Baima intrusion have the same color in the EBSD orientation map, indicating that each olivine grain has one dominant crystallographic orientation (Fig. 8). It is also noted that the isolated P-rich bands and patches in a single olivine grain share the same crystallographic orientation with P-poor olivine domains (Figs. 8e and f).

5. Discussion

5.1. Slow diffusion of P in olivine

Phosphorus can be incorporated into olivine through multiple substitution mechanisms. In most cases, P^{5+} is considered to substitute Si^{4+} in the tetrahedral site of olivine. The charge can be balanced by the vacancy on the M site: $4^{IV}P^{5+} + {}^{IV}[\text{vacancy}] = 5^{IV}Si^{4+}$ (Agrell et al., 1998) or $2^{IV}P^{5+} + 3^{VI}M^{2+} + {}^{VI}[\text{vacancy}] = 2^{IV}Si^{4+} + 4^{VI}M^{2+}$, where IV and VI refer to the tetrahedral and octahedral sites, respectively, and M^{2+} refers to divalent cations in the olivine lattice (Boesenberg and Hewins, 2010). Phosphorus could also be incorporated into olivine by a coupled substitution of P and trivalent elements, Al and Cr, for instance, $^{IV}Si^{4+} + 5^{VI}M^{2+} = {}^{IV}P^{5+} + 2^{IV}Al^{3+} + {}^{IV}Cr^{3+} + 2^{VI}$ [vacancy] (Milman-Barris et al., 2008). In this case, positive correlations of Al and Cr with P would be expected.

The diffusion coefficient of P in olivine (Fo_{90}) varies from $\sim 10^{-19}$ m^2/s at 1100 °C to $\sim 10^{-20}$ m^2/s at 900 °C (Watson et al., 2015). The diffusion coefficients of Ca and Cr are one order of magnitude higher than P, and those of Fe and Mg are two to four orders of magnitude higher than P at the same temperature

Table 1
Representative compositions of major, minor and trace element compositions of olivine from the Abulangdang and Baima intrusions, SW China.

Sample	DC1113 (Abulangdang)						DC1102 (Abulangdang)			
Rock-type	Lherzolite						Dunite			
Analysis No.	1–1	1–2	1–3	1–4	1–5	1–12	3–27	3–28	3–29	3–30
Analysis position	P-poor domain	P-poor domain	P-rich zone	P-rich zone	P-rich zone	P-rich zone	P-poor domain	P-poor domain	P-rich zone	P-rich zone
Major element oxides (wt.%) by EPMA										
SiO_2	39.83	39.80	39.89	39.84	39.94	39.88	40.96	40.47	40.59	40.28
FeO	15.15	15.19	14.95	15.09	15.06	14.82	11.64	11.79	11.66	11.58
MgO	44.26	44.29	44.42	44.44	44.90	44.93	47.09	46.82	47.29	46.90
NiO	0.34	0.29	0.33	0.33	0.34	0.33	0.37	0.35	0.35	0.33
CaO	0.04	0.08	0.05	0.04	0.07	0.05	0.09	0.06	0.08	0.07
Total	99.62	99.65	99.64	99.73	100.30	100.01	100.14	99.50	99.96	99.17
Fo (mol.%)*	84	84	84	84	84	84	88	88	88	88
Minor and trace elements (ppm) by LA-ICP-MS										
P	77.6	69.4	131	217	123	178	51.5	59.4	94.9	105
Mn	1870	1836	1792	1789	1799	1803	1417	1373	1411	1374
Co	188	188	182	187	187	183	172	164	170	164
Ni	2911	2937	2894	2906	2963	2942	3108	3067	3169	3072

Sample	BM12-122 (Baima)									
Rock-type	Net-textured Fe–Ti oxide ore									
Analysis No.	1–1	1–2	1–3	1–4	1–5	1–7	1–8	1–9	1–10	1–11
Analysis position	P-poor domain	P-poor domain	P-poor domain	P-poor domain	P-poor domain	P-poor domain	P-rich zone	P-rich zone	P-rich zone	P-rich zone
Major elemental oxides (wt.%) by EPMA										
SiO_2	37.83	38.33	38.07	38.00	37.94	37.95	38.17	37.78	38.22	37.93
FeO	25.00	25.63	25.31	26.10	25.75	25.88	26.12	25.89	26.14	26.09
MgO	36.77	36.44	36.45	36.12	36.17	36.26	36.06	35.93	36.01	36.13
NiO	0.01	0.01	0.02	0.02	0.03	0.02	0.01	0.03	0.03	0.02
CaO	0.03	0.04	0.03	0.03	0.04	0.04	0.03	0.03	0.04	0.03
Total	99.65	100.45	99.88	100.26	99.91	100.15	100.40	99.66	100.43	100.19
Fo (mol.%)	72	72	72	71	71	71	71	71	71	71
Minor and trace elements (ppm) by LA-ICP-MS										
P	126	153	164	199	190	163	378	542	566	525
Mn	3516	3741	3755	3842	3779	3853	3790	3824	3855	3772
Co	180	187	193	194	192	193	194	194	196	189
Ni	233	238	238	241	239	242	244	245	244	240

* $Fo = 100 \times Mg/(Mg + Fe)$ in molar percentage.

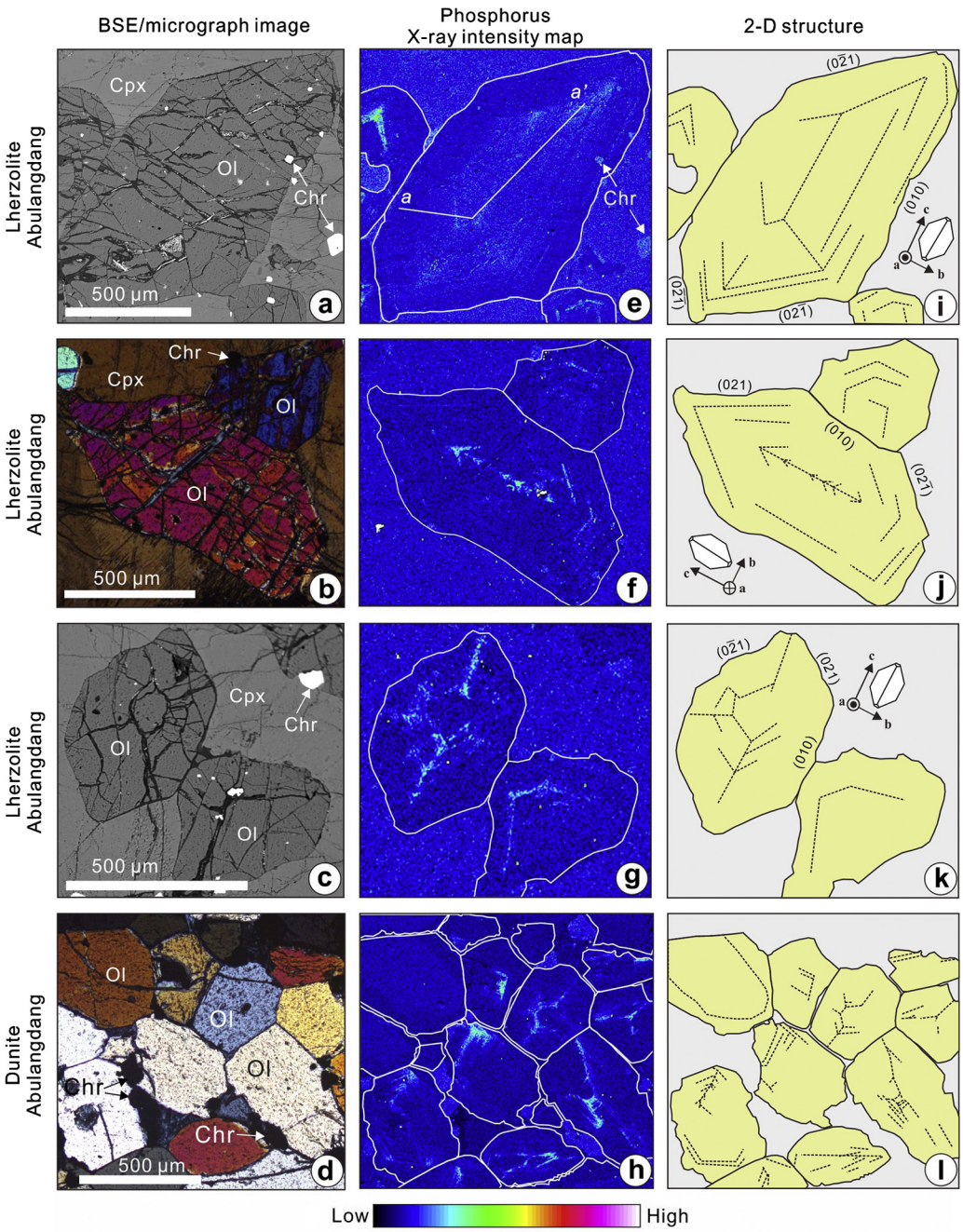

Fig. 4. Photomicrographs (a, b, c, d), X-ray phosphorus intensity maps (e, f, g, h) and reconstructed 2-D skeleton structures (i, j, k, l) for polyhedral olivine grains from lherlozite and dunite of the Abulangdang intrusion. Note that euhedral chromite is entrapped in P-poor olivine domain, and P-rich band close to chromite is straight and continuous. The 2-D structure of olivine was drawn based on the distribution of P-rich zones of olivine. Line a–a′ in Fig. 4e is the profile (Fig. 7a) for P concentration.

(Chakraborty, 2010; Watson et al., 2015). Therefore, phosphorus diffuses much slower than other elements in olivine. The nearly uniform intensities of Fe, Mg, Ca, Cr and Al and zonal distribution of P of olivine in our study are thus consistent with different diffusion coefficients of these elements (Supplementary Figs. 1 and 2). We thus believe that the distinctly different P zoning patterns of polyhedral and rounded olivine grains from the Abulangdang and Baima intrusions may record different growth processes in deep-seated magma chambers.

5.2. Origin of P zoning of polyhedral olivine

Olivine phenocrysts in volcanic rocks have banded, concentric, feathery or dendritic P zoning patterns (Milman-Barris et al., 2008; McCanta et al., 2008; Welsch et al., 2013, 2014). Primary P-rich zones are typically straight and continuous along the crystal faces of olivine and P-rich vertices propagate from the center of the crystal to its apexes, consistent with initially rapid, diffusion-controlled growth (Welsch et al., 2014). In our study, polyhedral olivine grains from dunite and lherzolite of the Abulangdang intrusion have P-rich dendrites identical to those observed in volcanic rocks (Fig. 4). We thus consider that olivine grains from the Abulangdang intrusion may have formed in a manner similar to olivine phenocrysts in volcanic rocks.

P-rich dendrites can grow rapidly if supersaturation of olivine in melts or high growth rate driven by rapid cooling occurs, in these cases, the crystal growth is far out of equilibrium (Donaldson, 1976; Welsch et al., 2014). The presence of P-rich dendrites

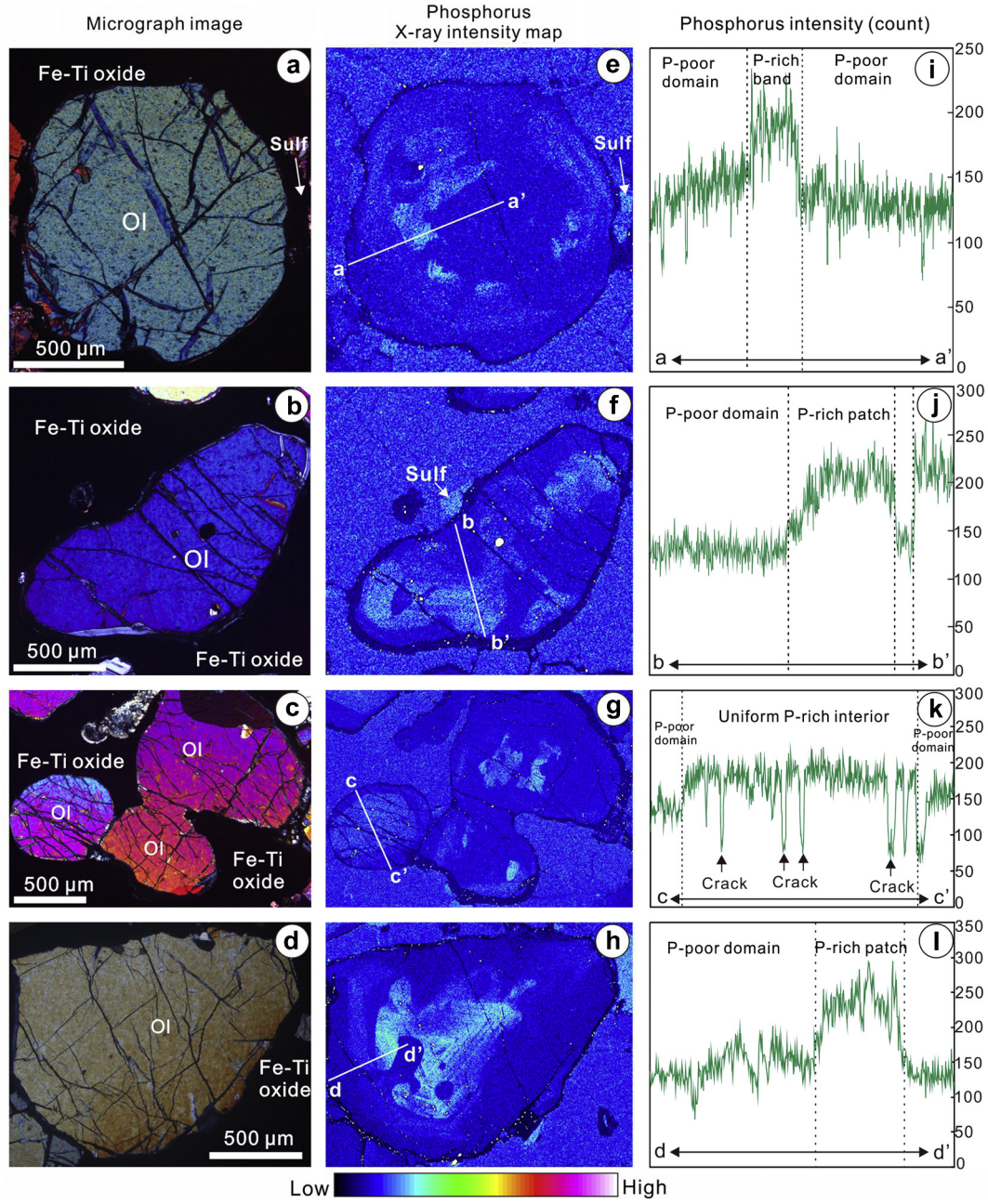

Fig. 5. X-ray phosphorus intensity maps and line scan analyses of rounded olivine grains from net-textured Fe–Ti oxide ores of the Baima layered intrusion. (a)–(d) Photomicrographs of net-textured Fe–Ti oxide ores showing rounded olivine (Ol) grains are enclosed in interconnected matrix of Fe–Ti oxides and sulfide (Sulf). Under cross-polarizer and transmitted light. (e)–(h) X-ray P intensity maps showing that concentric P-rich bands are crosscut by P-poor olivine domains (e), highly irregular P-rich patches are interlinked to each other and surrounded by P-poor olivine domains (f), uniform P-rich grain is surrounded by P-poor rim (left grain on g), P-rich patches are isolated by P-poor olivine domains (right grains on g) and skeletal, P-rich branches composed of closely spaced, P-rich thin bands (h). Note that sulfide next to olivine shows high P intensity due to element interference in image (f). (i)–(l) X-ray P intensity line scan analyses across P-rich band/patch and P-poor olivine domains.

in polyhedral olivine grains from the Abulangdang intrusion is thus indicative of disequilibrium growth. Similar P-rich dendrites were reported previously in two olivine grains in igneous cumulates, one is in a gabbro sample from the Mid-Atlantic Ridge and the other is in a harrisite sample from Rum Island of Scotland (Welsch et al., 2014). It is thus likely that the formation of cumulus olivine from mafic–ultramafic intrusions may have involved rapid growth so that P-rich dendrites could be formed in a deep-seated magma chamber. However, this stage of rapid growth is not recorded by nearly homogeneous compositions of major and some minor elements because of their fast diffusion (Fig. 7).

5.3. A two-stage growth model for rounded olivine from net-textured Fe–Ti oxide ores

The complex P zoning patterns of rounded olivine grains from net-textured Fe–Ti oxide ores of the Baima intrusion are distinctly different from that of P-rich dendrites in polyhedral olivine grains from the Abulangdang intrusion. Of particular significance are the embayment and curved boundaries of P-rich patches in rounded olivine grains (Figs. 5 and 6), typical of a disequilibrium texture. Concentric or irregular P-rich zones of olivine from spinel peridotite xenoliths in Anakies, SE Australia, were attributed to P-rich agent metasomatism and subsequent re-crystallization due to de-

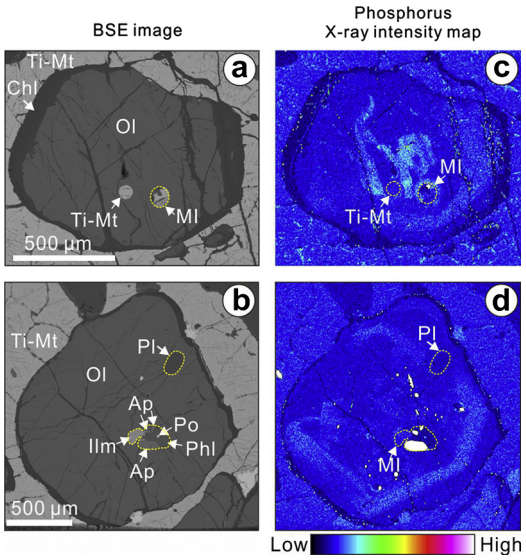

Fig. 6. BSE images (a, b) and X-ray P intensity maps (c, d) for rounded olivine from net-textured Fe–Ti oxide ores of the Baima layered intrusion. Note that rounded Ti-rich magnetite (Ti-Mt) and melt inclusion (MI) are completely entrapped in P-poor olivine domains or partly in contact with P-rich patches, and that P-rich patches near Ti-rich magnetite and melt inclusions are fairly irregular.

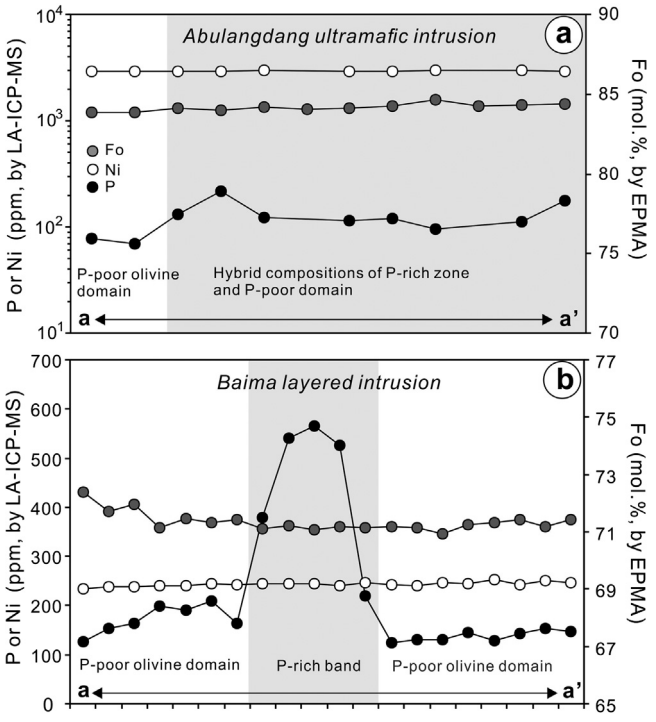

Fig. 7. Profiles of Fo, Ni and P concentrations of olivine from lherzolite of the Abulangdang intrusion (a) and net-textured Fe–Ti oxide ores of the Baima layered intrusion (b) showing that abrupt changes of P concentrations between P-rich bands/patches and P-poor olivine domains against relatively constant Fo and Ni within the same grain. Slightly high Fo content in the rims of olivine from the Baima intrusion is attributed to the Fe–Mg re-equilibration between olivine and interstitial Fe–Ti oxides. The profile a–a′ in Fig. 7a is shown in Fig. 4e and the profile a–a′ in Fig. 7b is shown in Fig. 5e.

formation (Mallmann et al., 2009). However, rounded olivine grains from net-textured Fe–Ti oxide ores of the Baima intrusion were not strongly deformed. In addition, skeletal, P-rich branches in rounded olivine grains (Fig. 5h) are considered to be primary skeleton formed initially by rapid growth (Welsch et al., 2014).

The embayment and curved boundaries of P-rich bands/patches in rounded olivine grains can be attributed to the resorption of P-rich bands/patches by P-poor olivine domains (cf., Milman-Barris et al., 2008). This may explain the diverse P zoning patterns of rounded olivine grains from net-textured ores of the Baima intrusion. Dissolution of primary olivine is possible if chemical disequilibrium occurs between olivine and an ambient melt (cf., Thornber and Huebner, 1985). In this scenario, P-rich bands and patches are likely the relicts of primary olivine that crystallized from the parental magma of the intrusion, whereas P-poor olivine domains could have crystallized from the ambient melt, which was not in equilibrium with primary olivine.

The isolated P-rich bands and patches in any rounded olivine grain have identical crystallographic orientation in the EBSD maps (Figs. 8e and f), indicating that they were remnants of the same

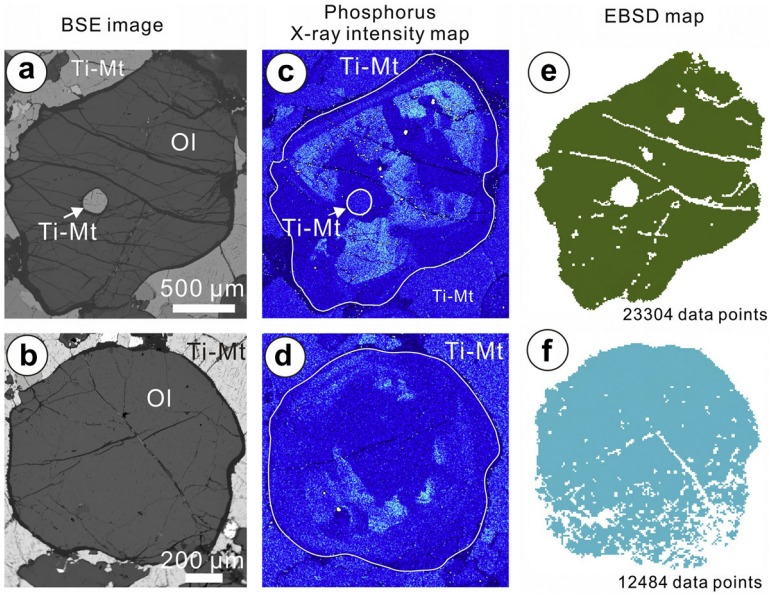

Fig. 8. BSE images (a, b), X-ray phosphorus intensity maps (c, d) and electron backscattered diffraction (EBSD) orientation maps (e, f) for rounded olivine grains from net-textured Fe–Ti oxide ores of the Baima layered intrusion. Each pixel represents an orientation derived from a diffraction pattern. Note that P-rich patches/bands and P-poor olivine domains overall have the same color. The white areas in the orientation maps were unidentified because of mineral inclusions, cracks and ragged surface in local places.

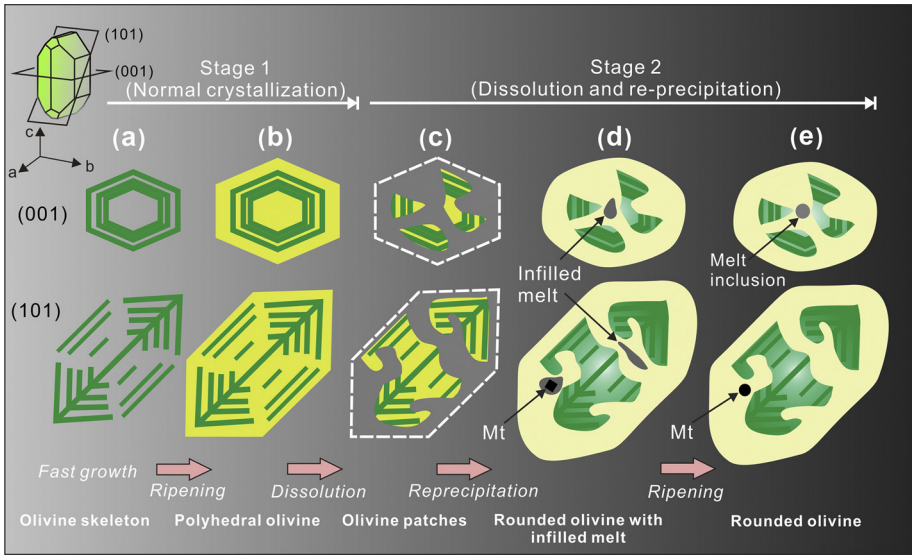

Fig. 9. A schematic cartoon illustrating a two-stage growth process of rounded olivine from net-textured Fe–Ti oxide ore of the Baima layered intrusion. **(1) First-stage growth**: (a) Rapid growth of skeletal or dendritic olivine from parental magmas. The shape of P-rich skeleton in (001) and (101) sections refers to Welsch et al. (2013). (b) Olivine skeleton gradually developed into polyhedral olivine with regular P zoning, which can be inferred to normal products of crystallization in igneous cumulates elsewhere, e.g., the Abulangdang intrusion. **(2) Second-stage growth**: (c) First-stage polyhedral olivine was partially dissolved by an Fe- and H_2O-rich ambient melt due to chemical disequilibrium. Regular P zoning was broken into pieces and only some remnants of primary crystals were preserved. (d) Re-precipitation from the ambient melt around the remnants of primary crystals formed P-poor olivine domains that inherited the crystallographic orientation of the primary olivine crystal. Fine-grained, Ti-rich magnetite and infilled melt were also entrapped into P-poor olivine domains in this stage. (e) The infilled melt and ambient melt both promoted the rounding of enclosed Ti-rich magnetite and host olivine by thermodynamic adjustment.

crystal. The identical crystallographic orientation between P-rich bands/patches and P-poor olivine domains in the same grain further indicates that re-precipitation of olivine likely inherited the preferred orientation of a primary olivine crystal (cf., Wheeler et al., 2001).

Based on the X-ray maps for P intensities of cumulus olivine grains in this study, we propose a two-stage growth model to explain the formation of rounded olivine grains from net-textured Fe–Ti oxide ores of the Baima intrusion. The first stage began with rapid growth of skeletal or dendritic olivine from the parental magma (Fig. 9a). The olivine dendrites gradually developed into polyhedral olivine with regular P zoning (Fig. 9b). The second stage was triggered by chemical disequilibrium so that the first-stage olivine was resorbed by an ambient melt (Fig. 9c). The first-stage olivine may have been partially dissolved by the ambient melt and thus regular P-rich bands were broken into irregular patches (Fig. 9c), and only some remnants of the primary olivine crystal were preserved. At the same time, slow re-precipitation of olivine from the ambient melt in hollowed, first-stage olivine formed the second-stage, P-poor olivine domains along the same crystallographic orientation of the primary olivine crystal (Fig. 9d).

Fine-grained Ti-rich magnetite and melt inclusions are entrapped in the embayment of P-poor olivine domains of rounded olivine grains from the Baima intrusion (Figs. 6c and 8c). Likewise, fine-grained chromite inclusions are enclosed within P-poor olivine domains in polyhedral olivine grains from the Abulangdang intrusion (Fig. 4e), and melt inclusions are all enclosed in P-poor domains of polyhedral olivine phenocrysts in volcanic rocks (Milman-Barris et al., 2008; Welsch et al., 2014). However, a remarkable difference among them is that P-rich zones near chromite and melt inclusions in polyhedral olivine from the Abulangdang intrusion and volcanic rocks are commonly regular and continuous (Fig. 4e), whereas P-rich patches near Ti-rich magnetite and polycrystalline inclusions in rounded olivine from the Baima intrusion are fairly irregular (Figs. 6c and 8c). This indicates that the entrapment of mineral and melt inclusions in rounded olivine grains may occur during partial dissolution of primary olivine and formation of melt embayment (cf., Borisova et al., 2014).

In our model, first-stage polyhedral olivine crystals may grow as dendritic forms like those in the Abulangdang intrusion. Fine-grained Ti-rich magnetite and melt inclusions in P-poor olivine domains were actually entrapped in the second-stage growth of olivine (Fig. 9d). In addition, Ti-rich magnetite inclusions in rounded olivine grains from net-textured Fe–Ti oxide ores of the Baima intrusion have compositions identical to Ti-rich magnetite interstitial to olivine (Liu et al., 2014b), and they thus were not early phases crystallized from the parental magma. This is against the conventional thought that enclosed minerals usually crystallized earlier than or concurrent with host minerals. Therefore, the crystallization sequence of mafic magmas based on textural relationships should be treated with caution.

5.4. Implications for magmatic processes to form Fe–Ti oxide-rich layered intrusions

Olivine from net-textured Fe–Ti oxide ores of the Baima intrusion has Fo contents ranging from 71 to 75 mol.% (Supplementary Table 3), and the parental magma of the intrusion was considered to resembles the Emeishan high-Ti flood basalts (Shellnutt et al., 2009). We assume that the ambient melt that was responsible for the second-stage olivine growth may have compositions equivalent to the polycrystalline inclusions enclosed within P-poor olivine domains. The polycrystalline inclusions contain abundant Fe–Ti oxides and phlogopite (Figs. 3d, and 6b, c and d), clearly indicative of crystallization from hydrous, Fe-rich magmas. Therefore, the ambient melt is estimated to be Fe- and H_2O-rich. Such a melt may behave as a medium in rounding process through thermodynamic adjustment (Watson and Brenan, 1987; Waff and Faul, 1992), because the presence of water does not favor growth of angularities on crystals, but favor round indentation and granular, bizarre-looking crystals, rather than facetted, angular crystals (Donaldson, 1976). This may explain why both fine-grained Ti-rich magnetite and host olivine have peculiar rounded morphologies (Fig. 3b).

Fe-rich ambient melt is distinctly different from the parental magma with high-Ti basaltic compositions. One possibility to gen-

erate such a melt is silicate liquid immiscibility within a crystal mush, a process that was proposed for the Baima intrusion and the Skaergaard intrusion in Greenland (Holness et al., 2011; Liu et al., 2014b). After the onset of immiscibility in the interstitial liquid, a preferential removal of a Si-rich conjugate melt could leave behind reactive Fe-rich melt interstitial to early phases (Holness et al., 2011). In the Baima intrusion, such early phases are the first-stage polyhedral olivine grains that crystallized from the parental magmas. Because of highly chemical disequilibrium between the ambient melt and polyhedral olivine, dissolution of polyhedral olivine and subsequent re-precipitation may have occurred. The Fe-rich ambient melt was also in chemical disequilibrium with other early phases such as plagioclase primocrysts in net-textured Fe–Ti oxide ores, consistent with the fact that the plagioclase grains were intensely resorbed and rimmed by amphibole (Fig. 3a).

The disequilibrium growth of olivine in this study is analogue to the growth of olivine in an experimental study of type I (Mg# $>$ 0.9) and type II (Mg# $<$ 0.9) chondrules, which shows that dissolved FeO in an ambient melt promoted the dissolution of magnesian olivine and ferroan olivine crystallized as overgrowths on the remaining forsterite grains (relicts) (Villeneuve et al., 2015). Our study therefore indicates that crystal growth triggered by chemical disequilibrium may be an important process for olivine growth in Fe–Ti oxide-rich layered intrusions. In turn, the disequilibrium textures in rounded olivine grains are important and unique records of an Fe-rich component that had ever developed in a crystal mush by silicate liquid immiscibility, rather than by crystal fractionation.

6. Conclusions

P-rich dendrites of polyhedral olivine in igneous cumulates of the Abulangdang intrusion challenge the conventional, tree-ring model of crystal growth in a slow-cooling magma chamber. Complex P zoning patterns of rounded olivine grains from net-textured Fe–Ti oxide ores of the Baima layered intrusion are unusual disequilibrium textures in igneous cumulates. Olivine growth induced by chemical disequilibrium may be an important process in Fe–Ti oxide-rich layered intrusions associated with the Fe enrichment of high-Ti basaltic magmas. The disequilibrium textures not only reveal two-stage growth of olivine, but also shed lights on the process of silicate liquid immiscibility in the formation of Fe–Ti oxide ores in layered intrusions. This study also shows that mineral and melt inclusions that are entrapped in P-poor olivine domains may not be early phases crystallized from parental magmas. Therefore, the crystallization sequence of mafic magmas based on textural relationships should be treated with caution. We thus argue that using core-rim compositional variations of olivine to extract the time scales of magmatic processes in magma chambers is not always reliable.

Acknowledgements

This study was financially supported by the Strategic Priority Research Program (B) of the Chinese Academy of Sciences (XDB18000000), NFSC grants Nos. 41325006, 41473017 and 41502048. We thank Yuxiao Ma for the assistance in the field trips in the Panxi region. We are grateful to Benoit Welsch and three anonymous reviewers, and editor, Michael Bickle, who kindly provided constructive comments that improved the quality of the manuscript. Mei-Fu Zhou is thanked for great help in improving English of the manuscript.

Appendix A. Supplementary material

Supplementary material related to this article can be found online at http://dx.doi.org/10.1016/j.epsl.2017.09.005.

References

Agrell, S., Charnley, N., Chinner, G., 1998. Phosphoran olivine from Pine Canyon, Piute Co., Utah. Mineral. Mag. 62, 265–269.
Barnes, S.J., 1986. The effect of trapped liquid crystallization on cumulus mineral compositions in layered intrusions. Contrib. Mineral. Petrol. 93, 524–531.
Boesenberg, J.S., Hewins, R.H., 2010. An experimental investigation into the metastable formation of phosphoran olivine and pyroxene. Geochim. Cosmochim. Acta 74, 1923–1941.
Borisova, A.Y., Faure, F., Deloule, E., Grégoire, M., Béjina, F., De Parseval, P., Devidal, J.-L., 2014. Lead isotope signatures of Kerguelen plume-derived olivine-hosted melt inclusions: constraints on the ocean island basalt petrogenesis. Lithos 198, 153–171.
Burton, W.K., Cabrera, N., Frank, F., 1951. The growth of crystals and the equilibrium structure of their surfaces. Philos. Trans. R. Soc. Lond. Ser. A, Math. Phys. Sci. 243, 299–358.
Chakraborty, S., 2010. Diffusion coefficients in olivine, wadsleyite and ringwoodite. Rev. Mineral. Geochem. 72, 603–639.
Donaldson, C.H., 1976. An experimental investigation of olivine morphology. Contrib. Mineral. Petrol. 57, 187–213.
Faure, F., Schiano, P., Trolliard, G., Nicollet, C., Soulestin, B., 2007. Textural evolution of polyhedral olivine experiencing rapid cooling rates. Contrib. Mineral. Petrol. 153, 405–416.
Faure, F., Schiano, P., 2005. Experimental investigation of equilibration conditions during forsterite growth and melt inclusion formation. Earth Planet. Sci. Lett. 236, 882–898.
Faure, F., Schiano, P., 2004. Crystal morphologies in pillow basalts: implications for mid-ocean ridge processes. Earth Planet. Sci. Lett. 220, 331–344.
Faure, F., Trolliard, G., Nicollet, C., Montel, J.-M., 2003. A developmental model of olivine morphology as a function of the cooling rate and the degree of undercooling. Contrib. Mineral. Petrol. 145, 251–263.
Helz, R.T., 1987. Diverse olivine types in lava of the 1959 eruption of Kilauea volcano and their bearing on eruption dynamics. U. S. Geol. Surv. Prof. Pap. 1350, 691–722.
Holness, M.B., Stripp, G., Humphreys, M.C.S., Veksler, I.V., Nielsen, T.F.D., Tegner, C., 2011. Silicate liquid immiscibility within the crystal mush: late-stage magmatic microstructures in the Skaergaard intrusion, East Greenland. J. Petrol. 52, 175–222.
Jambon, A., Lussiez, P., Clocchiatti, R., Weisz, J., Hernandez, J., 1992. Olivine growth rates in a tholeiitic basalt: an experimental study of melt inclusions in plagioclase. Chem. Geol. 96, 277–287.
Li, H., Zhang, Z., Santosh, M., Lü, L., Han, L., Liu, W., 2017. Late Permian basalts in the Yanghe area, eastern Sichuan Province, SW China: implications for the geodynamics of the Emeishan flood basalt province and Permian global mass extinction. J. Asian Earth Sci. 134, 293–308.
Liu, P.-P., Zhou, M.-F., Wang, C.Y., Xing, C.-M., Gao, J.-F., 2014a. Open magma chamber processes in the formation of the Permian Baima mafic–ultramafic layered intrusion, SW China. Lithos 184, 194–208.
Liu, P.-P., Zhou, M.-F., Chen, W.T., Boone, M., Cnudde, V., 2014b. Using multiphase solid inclusions to constrain the origin of the Baima Fe–Ti-(V) oxide deposit, SW China. J. Petrol. 55, 951–976.
Liu, Y., Hu, Z., Gao, S., Günther, D., Xu, J., Gao, C., Chen, H., 2008. In situ analysis of major and trace elements of anhydrous minerals by LA-ICP-MS without applying an internal standard. Chem. Geol. 257, 34–43.
Mallmann, G., O'Neill, H.S.C., Klemme, S., 2009. Heterogeneous distribution of phosphorus in olivine from otherwise well-equilibrated spinel peridotite xenoliths and its implications for the mantle geochemistry of lithium. Contrib. Mineral. Petrol. 158, 485–504.
McCanta, M., Beckett, J., Stolper, E., 2008. Zonation of phosphorus in olivine: dynamic crystallization experiments and a study of chondrule olivine in unequilibrated ordinary chondrites. Lunar Planet. Sci. Conf., 1807.
Milman-Barris, M.S., Beckett, J.R., Baker, M.B., Hofmann, A.E., Morgan, Z., Crowley, M.R., Vielzeuf, D., Stolper, E., 2008. Zoning of phosphorus in igneous olivine. Contrib. Mineral. Petrol. 155, 739–765.
Pang, K.-N., Zhou, M.-F., Qi, L., Shellnutt, G., Wang, C.Y., Zhao, D., 2010. Flood basalt-related Fe–Ti oxide deposits in the Emeishan large igneous province, SW China. Lithos 119, 123–136.
Pang, K.-N., Zhou, M.-F., Lindsley, D., Zhao, D., Malpas, J., 2008. Origin of Fe–Ti oxide ores in mafic intrusions: evidence from the Panzhihua Intrusion, SW China. J. Petrol. 49, 295–313.
Pilbeam, L.H., Nielsen, T., Waight, T.E., 2013. Digestion fractional crystallization (DFC): an important process in the genesis of kimberlites. Evidence from olivine in the Majuagaa kimberlite, southern West Greenland. J. Petrol. 54, 1399–1425.
Qi, L., Wang, C.Y., Zhou, M.-F., 2008. Controls on the PGE distribution of Permian Emeishan alkaline and peralkaline volcanic rocks in Longzhoushan, Sichuan Province, SW China. Lithos 106, 222–236.
Sanfilippo, A., Tribuzio, R., Tiepolo, M., 2014. Mantle–crust interactions in the oceanic lithosphere: constraints from minor and trace elements in olivine. Geochim. Cosmochim. Acta 141, 423–439.
Spandler, C., O'Neill, H.S.C., Kamenetsky, V.S., 2007. Survival times of anomalous melt inclusions from element diffusion in olivine and chromite. Nature 447, 303–306.

Shellnutt, J.G., Iizuka, Y., 2012. Oxidation zonation within the Emeishan large igneous province: evidence from mantle-derived syenitic plutons. J. Asian Earth Sci. 54–55, 31–40.
Shellnutt, J.G., Zhou, M.-F., Zellmer, G.F., 2009. The role of Fe–Ti oxide crystallization in the formation of A-type granitoids with implications for the Daly gap: an example from the Permian Baima igneous complex, SW China. Chem. Geol. 259, 204–217.
Sobolev, A.V., Hofmann, A.W., Kuzmin, D.V., Yaxley, G.M., Arndt, N.T., Chung, S.-L., Danyushevsky, L.V., Elliott, T., Frey, F.A., Garcia, M.O., 2007. The amount of recycled crust in sources of mantle-derived melts. Science 316, 412–417.
Thornber, C.R., Huebner, J.S., 1985. Dissolution of olivine in basaltic liquids: experimental observations and applications. Am. Mineral. 70, 934–945.
Villeneuve, J., Libourel, G., Soulié, C., 2015. Relationships between type I and type II chondrules: implications on chondrule formation processes. Geochim. Cosmochim. Acta 160, 277–305.
Waff, H.S., Faul, U.H., 1992. Effects of crystalline anisotropy on fluid distribution in ultramafic partial melts. J. Geophys. Res. 97, 9003–9014.
Wang, C.Y., Zhou, M.-F., Yang, S., Qi, L., Sun, Y., 2014. Geochemistry of the Abulangdang intrusion: cumulates of high-Ti picritic magmas in the Emeishan large igneous province, SW China. Chem. Geol. 378, 24–39.
Watson, E.B., Cherniak, D., Holycross, M., 2015. Diffusion of phosphorus in olivine and molten basalt. Am. Mineral. 100, 2053–2065.
Watson, E.B., Brenan, J.M., 1987. Fluids in the lithosphere, 1. Experimentally-determined wetting characteristics of CO_2–H_2O fluids and their implications for fluid transport, host-rock physical properties, and fluid inclusion formation. Earth Planet. Sci. Lett. 85, 497–515.
Welsch, B., Hammer, J., Hellebrand, E., 2014. Phosphorus zoning reveals dendritic architecture of olivine. Geology 42, 867–870.
Welsch, B., Faure, F., Famin, V., Baronnet, A., Bachèlery, P., 2013. Dendritic crystallization: a single process for all the textures of olivine in basalts? J. Petrol. 54, 539–574.
Wheeler, J., Prior, D., Jiang, Z., Spiess, R., Trimby, P., 2001. The petrological significance of misorientations between grains. Contrib. Mineral. Petrol. 141, 109–124.
Xu, H., Zhang, J., Yu, T., Rivers, M., Wang, Y., Zhao, S., 2015. Crystallographic evidence for simultaneous growth in graphic granite. Gondwana Res. 27, 1550–1559.
Xu, Y., Chung, S.-L., Jahn, B.-M., Wu, G., 2001. Petrologic and geochemical constraints on the petrogenesis of Permian–Triassic Emeishan flood basalts in southwestern China. Lithos 58, 145–168.
Zhou, M.-F., Arndt, N.T., Malpas, J., Wang, C.Y., Kennedy, A.K., 2008. Two magma series and associated ore deposit types in the Permian Emeishan large igneous province, SW China. Lithos 103, 352–368.
Zhou, M.-F., Robinson, P.T., Lesher, C.M., Keays, R.R., Zhang, C.-J., Malpas, J., 2005. Geochemistry, petrogenesis and metallogenesis of the Panzhihua gabbroic layered intrusion and associated Fe–Ti–V oxide deposits, Sichuan Province, SW China. J. Petrol. 46, 2253–2280.